50th AIAA Aerospace Sciences Meeting including the New Horizons Forum and Aerospace Exposition
09 - 12 January 2012, Nashville, Tennessee
AIAA 2012-0084

Visualization and Tracking of Vortices and Shear Layers in the Late Stages of Boundary-Layer Laminar-Turbulent Transition

Ulrich Rist[1]
Universität Stuttgart, Stuttgart, 70550, Germany

The purpose of this contribution is to present some examples for the use of recent data processing and visualization techniques for the study of unsteady vortical flows. The basic idea is to extract vortices, shear layers and data defining their current state from DNS data and to track their evolution in time. Some apparent signatures which help to get additional insight into the flow dynamics have been identified. They demonstrate the promising features of the technique, albeit further studies are necessary to complete this work.

Nomenclature

I_2	=	second invariant of the strain-rate tensor
L	=	reference length
P	=	enstrophy production rate
p	=	fluid pressure
Re	=	Reynolds number $U_\infty L/\nu$
Re^*	=	displacement-thickness Reynolds number $U_\infty \delta^*/\nu$
$\boldsymbol{S}$	=	strain-rate tensor (symmetric part of the velocity-gradient tensor)
S_{ij}	=	element of the strain-rate tensor
S_{HK}	=	scalar for shear layer identification proposed by Haimes & Kenwright[11]
t_p	=	normalized phase angle with respect to the forcing cycle ($0 \le t_p \le 1$)
u_{ind}	=	induced velocity computed from the Biot-Savart law
U_∞	=	Free-stream speed
i, j	=	indices of tensor elements according to Einstein's summation convention $1 \le i, j \le 3$
X, Y, Z	=	streamwise, wall-normal, and spanwise coordinate direction, resp.
u, v, w	=	streamwise, wall-normal, and spanwise velocity component, resp.
$\lambda_1, \lambda_2, \lambda_3$	=	ordered eigenvalues of the tensor $\boldsymbol{\Omega}^2 + \boldsymbol{S}^2$, $\lambda_1 > \lambda_2 > \lambda_3$
λ_{ci}	=	complex part of eigenvalues of the velocity-gradient tensor
ω	=	vorticity (here, negative curl of velocity vector)
ω_x	=	streamwise vorticity component $\partial v/\partial z - \partial w/\partial y$
ω_z	=	spanwise vorticity component $\partial u/\partial y - \partial v/\partial x$
$\boldsymbol{\Omega}$	=	rotation tensor (anti-symmetric part of the velocity-gradient tensor)
$\nabla \boldsymbol{v}$	=	velocity-gradient tensor

I. Introduction

A typical feature of late-stage transitional flows and even of fully developed turbulence is the occurrence of elongated and ring-like vortical structures with adjacent high-shear layers. Previous studies based on wind-tunnel experiments[9], computer simulations[35], or both[1] helped to establish and corroborate this view. Nevertheless, despite their relevance, none of these studies has already delivered such a kind of breakthrough that laminar-turbulent transition and turbulence can be fully explained based on, e.g. vortex kinematics. The reasons for this could be that (a) the physics are simply too complicated and too complex, or (b), that we still lack the necessary understanding and description of the basic building blocks of a turbulent flow. In case (a) there is no foreseeable

[1] Professor, Institut für Aerodynamik und Gasdynamik, Pfaffenwaldring 21, 70550 Stuttgart, Germany, Associate Member AIAA.

way out. Case (b) is still under work. One way (b-i) is to investigate generic interactions of isolated vortices, work that has been started in the 1980s[16-18, 25], which delivered many interesting findings. But these findings and observations in generic cases should be identified and compared to transitional flows and turbulent flows trying to build a kinematical description of these more natural flows which are also more complex. The other way (b-ii) is to find and use new algorithms for identification, extraction, tracking and quantification of flow-field structures. The present work tries to follow this way.

Looking at existing studies of late-stage laminar-turbulent transition in boundary layers or at studies of the instantaneous flow field in a turbulent boundary layer, it turns out that most illustrations used to present the authors' findings are either hand-drawn sketches or user-selected visualizations of chosen flow-field data or derivatives thereof. One of our aims is to try to automate these processes using algorithms which were not available 20 years ago. As new measurement techniques and direct numerical simulations with ever increasing resolution and accuracy can provide more and more quantitative data to visualize flow features and to study their evolution and possible interactions, there is a clear need for automatization of the associated post-processing steps. Ideally, one would like to decompose any flow field into its basic structures, regardless of its complexity.

For many flows there is a clear preference for considering vortices as the most relevant basic flow-field structures. This could be due to observations in idealized configurations where the complete flow field can be reduced to its singularities and easily be recovered using vortex-induced velocities from the Biot-Savart law. The benefits of such a concept are tempting because of enormous data savings via data reduction and because of simplification of the problem by producing a mental picture on a higher level of abstraction than the mere raw data.

In the literature there has been a considerable debate about the merits and accuracies of different vortex-identification methods, see Refs. 5-8, 12, 14, 15, 21, 34, and 36, for instance. Users seem to prefer the Q-method which indicates presence of a vortex if the local rate of rotation is larger than the rate of strain[14], the "swirling strength"[1, 6] which is identical to the complex part of the eigenvalues of the velocity-gradient tensor which appears only in areas where the linearized flow field has a rotational component, or the λ_2-method[14] which tries to locate inflection points of a pressure field corrected by viscous and unsteady straining effects. Use of older criteria like pressure or vorticity is on the decline because of their apparent deficiencies. Nevertheless, these quantities are needed to verify if the identification performed by other methods is plausible. The only "objective" criterion, proposed by Haller[12] is prohibitively computing-time expensive and therefore not in widespread use.

Using visualization techniques it should be possible to observe and track the generation, convection, deformation and breakdown of vortices in the laminar-turbulent transition of a boundary-layer flow. However, for a deeper understanding of such visual observations it is necessary to go a step further and quantify the observations. One important aspect is the search for criteria which can be used to "alert" the observer when a certain "event" is about to occur. These events would be the generation of a vortex or a certain kind of interaction between neighboring vortices. The present paper will show some examples of our recent work on these topics applied to a late-stage transitional boundary-layer flow. It is organized as follows. We start with a description of the DNS data source in section II and we show results related to vortex identification, segmentation of vortices, vortex tracking and feature extraction along vortex axes in section III. Results of combining vortex with shear-layer visualization are presented in section IV, and the paper concludes with an outlook in section V.

II. DNS Data Source

For the present research we used DNS data of laminar-turbulent transition in an incompressible flat-plate boundary layer described in Ref. 2 where the complete three-dimensional, unsteady vorticity and velocity field have been computed. An overview of the available data space is provided in Figure 1 using contours and an iso-surface of the spanwise vorticity component *RZ*. *X, Y,* and *Z* are the streamwise, wall-normal, and spanwise coordinate directions, respectively. They are normalized with respect to a reference length L which enters into the Reynolds number $\mathrm{Re} = U_\infty L/\nu = 100000$, where U_∞ is the constant free-stream speed, and ν the kinematic viscosity of the fluid. The simulation set-up consists of a laminar base flow (Blasius solution) at inflow $X = 1.47$ and zero streamwise pressure gradient. The integration domain extends until $X = 4.73$ and periodic boundary conditions in spanwise direction are used at $Z = \pm 0.2$. The spanwise direction is discretized using 307 de-aliased fully complex spectral modes, such that the symmetry of the flow field with respect to the spanwise "peak" plane at $Z = 0$ can be broken by an appropriate asymmetric initial disturbance, see Ref. 27. The streamwise and wall-normal directions are discretized with 2730 equidistant and 201 non-equidistant grid points, respectively. Compact finite differences of sixth-order accuracy are used in the latter two directions and time integration is performed by an explicit fourth-order accurate Runge-Kutta scheme[20]. Harmonic disturbances are introduced via a spanwise disturbance strip centered at $X = 1.70$ (where the local displacement thickness Reynolds number is $\mathrm{Re}^* = 730$).

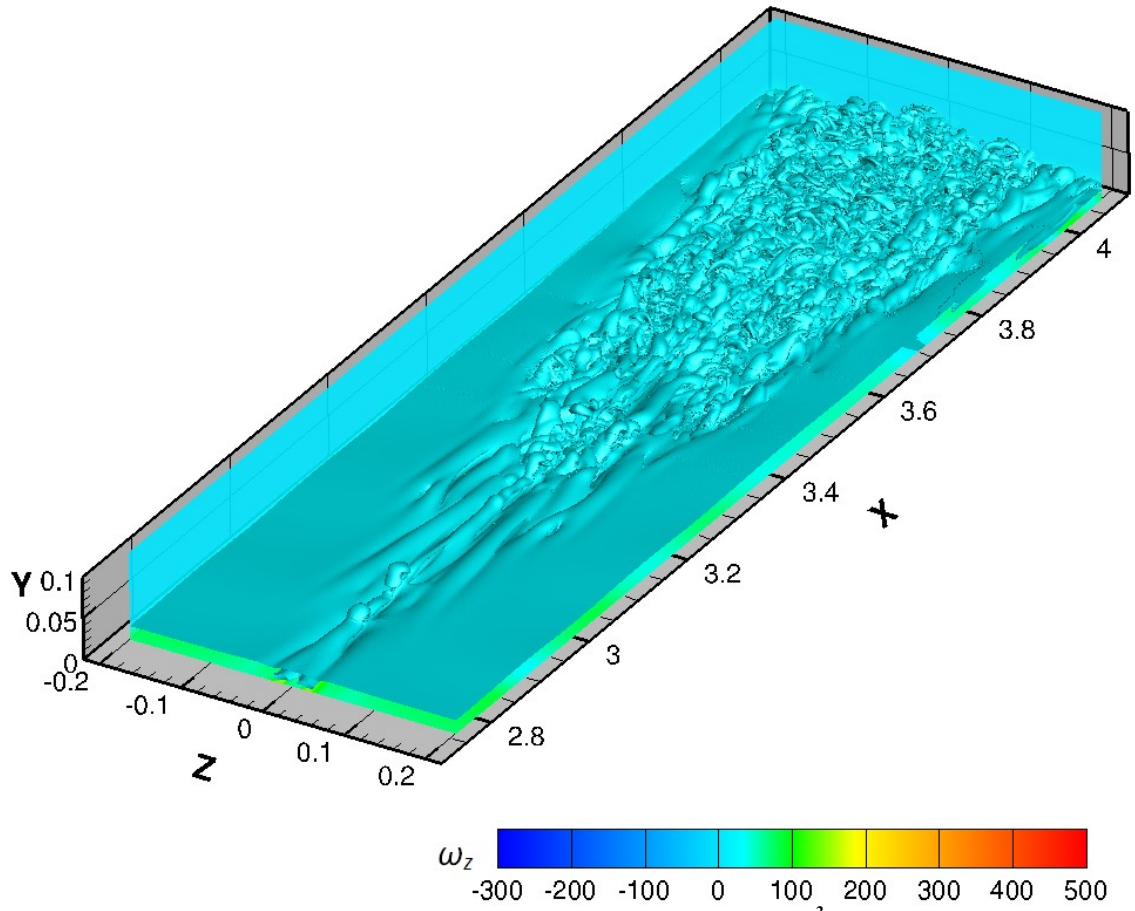

Figure 1. Snapshot of spanwise vorticity in the DNS data set of Bake *et al.*[2].

As the forcing consists of a two-dimensional Tollmien-Schlichting wave with a local high-amplitude "bump" or "seed" around $Z = 0$, see Ref. 2, the laminar-turbulent transition starts upstream in the central part of the domain, see Figure 1. The alternating green and blue vorticity pattern that can be seen on the wall depicts the TS-wave. Superposed is a turbulent wedge that starts from Λ-shaped vortices in the upstream part. Wall friction increases proportionally with spanwise vorticity and small-scale structures start to populate the boundary layer as the disturbances travel downstream. High- and low-speed streaks develop and animated data sequences show ejection and sweep events, as in a turbulent boundary layer[9, 28].

Explaining and understanding such complex physics are a challenge for research. What are the mechanisms at work? Which are the most relevant flow-field structures? How do they originate, evolve, interact and finally disappear? How to visualize and how to describe these effects? Which interactions among different structures play a role and how can one visualize, identify or quantify these?

We propose to study vortices and shear layers as basic structures of the boundary layer. Both items appear in other flows as well such that results related to their generation, interaction, etc. can be generic enough to be transferred to other cases or re-identified in the present scenario. We continue with a closer look on vortices in the next section before we present results of shear-layer identification.

III. Identification and Tracking of Vortices

Vortices are omnipresent in nature and engineering[24]. They appear from large scales like distant galaxies down to the smallest scales like dissipation of energy in a turbulent flow. One single vortex can control the flow surrounding it in a large area. Several vortices interact like a gear box. Vortices are at the origin of particle (vortex) methods which solve the Navier-Stokes equations in a Lagrangian frame[22]. It is therefore natural to start with vortices for a deeper exploration of the mechanisms in late-stage laminar-turbulent boundary-layer transition.

A. Vortices in a Transitional Boundary Layer

Many investigations have repeatedly shown that so-called hairpin vortices are a general feature of transitional and turbulent flows. This is especially true for the present scenario which is a variant of the so-called K-type scenario (named after the controlled experiments of Klebanoff *et al.*[19]), where the laminar-turbulent transition process in a zero streamwise-pressure-gradient boundary layer is initiated by introducing a large-amplitude Tollmien-Schlichting wave with prescribed spanwise periodicity using spanwise roughness elements. A characteristic of this scenario is the occurrence of spanwise "peak" and "valley" planes where the disturbance amplitudes are maximal or minimal, respectively. The coordinate system of the present data set is arranged such that the "peak" plane is situated at $Z=0$. To describe the flow-field structures in the following we shall use the terms Λ- and Ω-vortices introduced by Hama & Nutant[13] based on their hydrogen-bubble visualizations of such structures in a transitional boundary layer.

The hand-drawn sketches in Figure 2 depict three consecutive snapshots of the unsteady development of a Λ-vortex. All depicted structures are symmetric with respect to the spanwise "peak" plane. Velocities induced by the vortex on different sides of its axis are depicted by pairs of red and blue arrows. Subfigure a) illustrates that these motions produce an updraft between the legs of the Λ and a downdraft on the outside. Such motions are known to lead to low- and high-speed streamwise-velocity streaks close to the wall. Another observation is that the upward motion at the downstream loop of the Λ, see label "A" in the sketch, lifts the latter further away from the wall into an upright position, see label "B". As the streamwise flow is faster further away from the wall, a hairpin forms at the downstream end of the Λ and the counter-rotating legs get stretched in streamwise direction. After this, a "bridge" develops between the two, circle "C". The latter is a typical effect observed when two vortices interact, see Ref. 25. The new bridge develops into a new Ω-shape and becomes the new "head" of the Λ-vortex as the first hairpin snatches away from the Λ in c), circle "D".

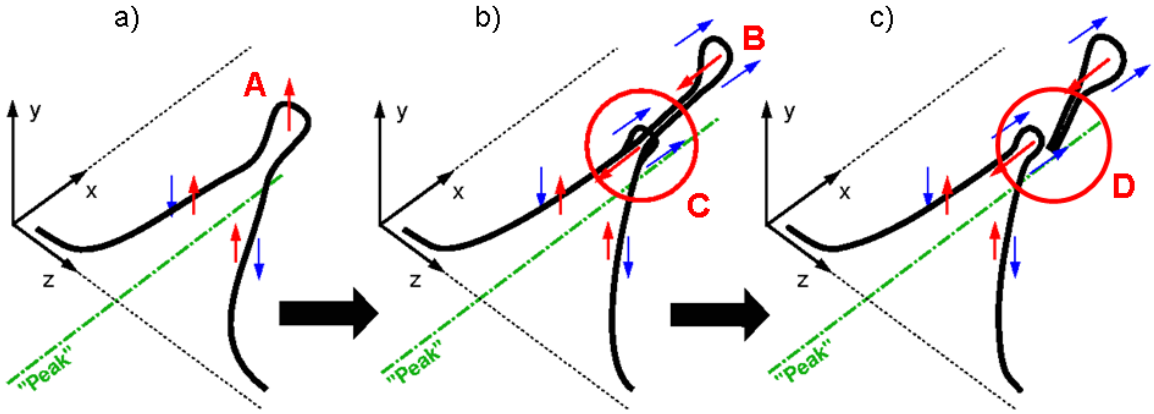

Figure 2. Idealized sketch of the evolution of a transitional Λ-vortex and generation of Ω-shaped hairpin vortices. Red and blue arrows depict vortex-induced motions on different sides of the axis. A new Ω-vortex starts as a "bridge" between the "legs" of the first Λ, see red circle C in b). Sketch originally from Sebastian Bake, Berlin.

B. Validation of Vortex Identification Methods for the Present Application

One motivation for the present work was to replace hand-drawn illustrations like those shown in Figure 2 by computer-generated images. Once validated for well-known cases this approach offers the potential of being applicable to much more complicated scenarios than just one or a few isolated vortices.

Many vortex-identification methods have been suggested since the pioneering paper on using invariants of the velocity-gradient tensor by Chong, Perry and Cantwell[7] see references 5, 6, 14, 15, 21 and 12, for instance. Following the arguments and examples given by Jeong & Hussain[14] our initial favorite became the λ_2-method. For this the velocity-gradient tensor $\nabla \boldsymbol{v}$ is computed for every grid point and split into its symmetric and anti-symmetric parts, $\boldsymbol{\Omega}$ and $\boldsymbol{S}$, respectively.

$$\nabla \boldsymbol{v} = \boldsymbol{\Omega} + \boldsymbol{S}. \tag{1}$$

The eigenvalues of the new tensor $\boldsymbol{\Omega}^2 + \boldsymbol{S}^2$ are computed and sorted such that $\lambda_1 > \lambda_2 > \lambda_3$. According to Ref. 14 vortices are then identified by regions of $\lambda_2 < 0$. In practice, isosurfaces $\lambda_2 = \delta_v$, with $\delta_v < 0$ are used to visualize such vortices. Other criteria which we used were pressure, vorticity, and the magnitude λ_{ci} of the imaginary part of the eigenvalues of the velocity-gradient tensor. The latter is also called "swirling strength" by Adrian[1] and Chakraborty *et al.*[6]

Figure 3 illustrates the position of a streamwise cutting plane used for validation of the λ_2-method. An iso-surface of λ_2 = const. visualizes a combined Λ-Ω-vortex comparable to the sketch in Figure 2 b). The cutting plane contains only contours for $\lambda_2 < 0$. Two distinct minima occur where the vortices are intersected by the plane. It is interesting and important to note that the gradient of λ_2 is very steep around $\lambda_2 = 0$. This makes the visualization output to a large extent independent of the chosen threshold, as long as the latter is not too close to the λ_2 minimum inside the vortex. The wall-normal cutting line at $x = 440$ *mm* will be used further down . Note that the data used for this section are not from the DNS of Bake *et al.*[2] but from an earlier one. This is why the coordinates are different from those used in the other sections.

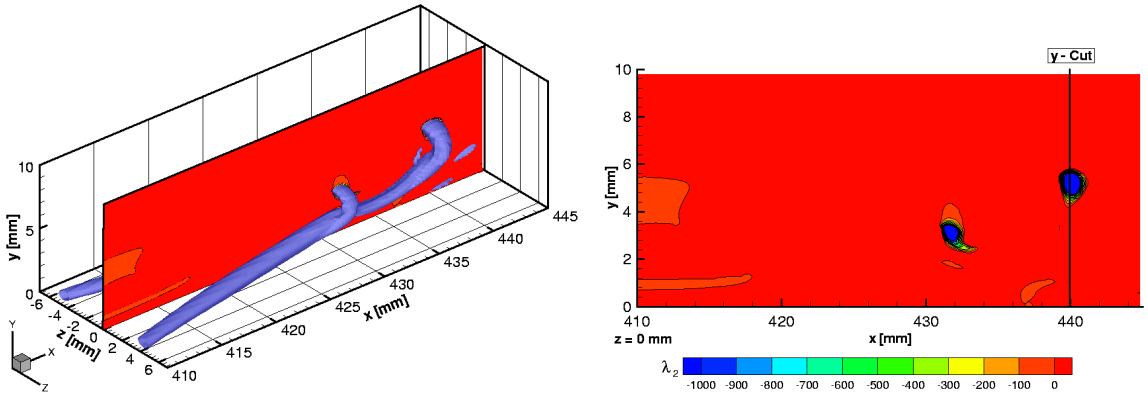

Figure 3. Vortex identification using the λ_2-method. Left: definition of the cutting plane at the spanwise peak station of the disturbance relative to an observed vortex. Right: contours of λ_2.

Comparing the contours of λ_2 with the contours of pressure and vorticity in Figure 4 shows that the negative λ_2 correlates well with local pressure minima which also indicate the presence of vortices. However the pressure gradients away from the vortex center are much weaker than the λ_2 gradients and the possible extent of the vortex is not as clear as before. Similar observations can be made by consulting the vorticity magnitude. There is a clear-cut local maximum of streamwise rotation at $x = 440$ *mm* where the downstream Ω is cut, but there is also a high-shear layer in addition to the high shear at the wall in the downstream part of the figure and the less concentrated shear of the laminar boundary layer in the upstream part. This is due to the problem that vorticity does not distinguish between shear layers and vortices. Again the extent of the vortices is less clear than in Figure 3. The bridge at $x = 434$ *mm* which is going to become the new head of the Λ-vortex later on, is not clearly discernable from the high-shear layer. Nevertheless, the latter starts to display a local maximum there.

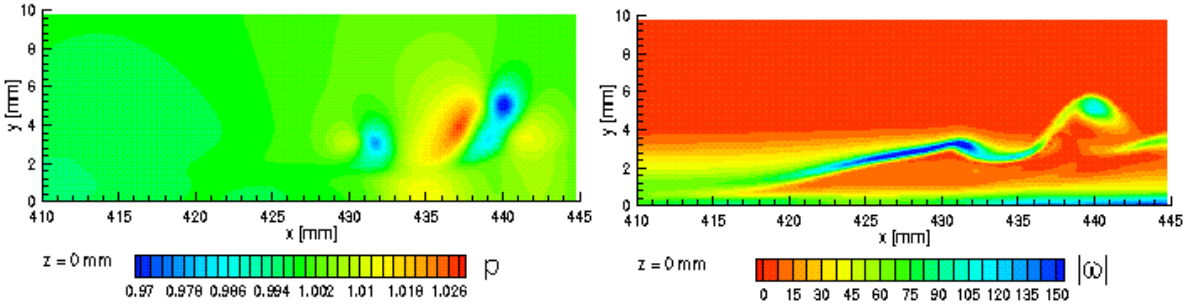

Figure 4. Comparison of pressure and vorticity magnitude in the peak plane.

A more quantitative insight into the performance of the λ_2-method can be obtained using wall-normal cuts through the data along the line $x = 440$ *mm* which cuts directly through the vortex center. All curves have been plotted such that the maxima of each quantity appear above the abscissa (as if they were positive) and are approximately equal enabling an easy and detailed comparison of different criteria. The curves of λ_2 and λ_{ci} (swirling strength) almost follow each other in the area of the main maximum. However, λ_{ci} shows some extra, smaller

maxima for smaller y. These do not belong to vortices because there is neither a local vorticity maximum nor a pressure minimum there. The comparison of λ_2 with the pressure curve confirms that the pressure inside the vortex is lower than in the ambient. Projecting the points $\lambda_2 = 0$ on the pressure curve indicates that the maximal extent of the vortex predicted by the λ_2-method corresponds to the distance between the inflection points of the pressure field (zeroes of the Hessian of the pressure field, as predicted by Jeong & Hussain[14]). The pressure at the positions of the inflection points is not the same on both sides of the vortex due to the presence of additional pressure gradients in the flow. There is a clear advantage of using λ_2 instead of pressure thresholds because the λ_2-method is not sensitive to such global gradients and less biased with respect to asymmetries and the chosen constant threshold.

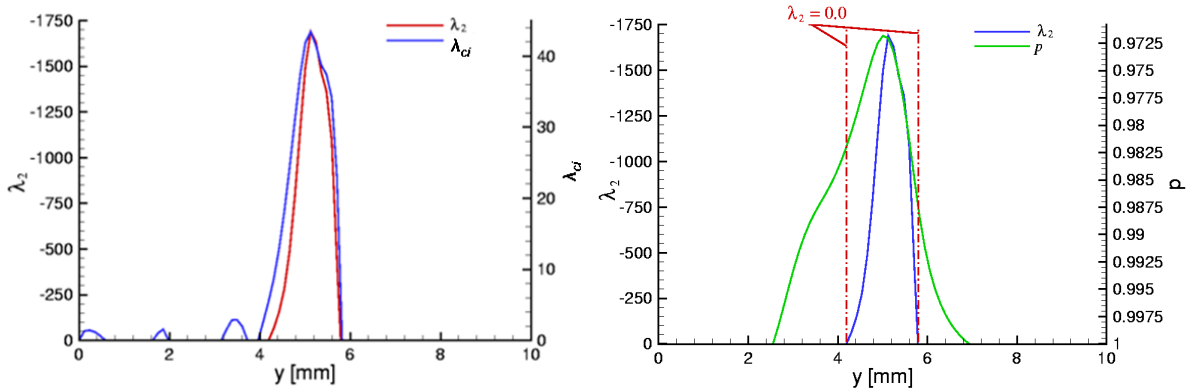

Figure 5. Comparison of the scalar vortex-identification criterion λ_2 with the magnitude of the imaginary part λ_{ci} of the eigenvectors of the velocity-gradient tensor (left), and with pressure (right).

The previous validations are complemented in the next two figures by similar comparisons using a spanwise cut at $x = const.$ cutting through the "legs" of the Λ, as illustrated in Figure 6. The presence of the Λ-vortex is again clearly indicated in this cut and also confirmed by pressure minima and streamwise vorticity maxima in Figure 7. The pressure field shows an extension of the low-pressure regions towards the wall. Reason for this is the condition $\partial p/\partial y = 0$ close to the wall resulting from the y-momentum equation at the wall. This leads to characteristic low-pressure footprints of the Λ-vortices on the wall. Another observation is that vorticity magnitude is not able to detect the vortex because of the presence of high (spanwise) shear which dominates over the streamwise vorticity. This is why the streamwise vorticity ω_x is consulted as well in Figure 7. The vorticity magnitude shows that strong high-shear layers develop above and below the Λ-vortex in agreement with the induced motions sketched in Figure 2. A closer look at the streamwise vorticity indicates that the local extremes due to streamwise vortices are almost surrounded by streamwise vorticity of the opposite sign. This can be explained by velocity gradients at the edge of the vortices which are caused by the fact that the circumferential velocity cannot increase forever away from the center of rotation. It must decay to zero farther away and the according velocity gradients show up as streamwise vorticity of opposite sign especially at the wall where the space for this velocity decay is limited by the no-slip condition at the wall. This leads to spanwise shear that is as large as the streamwise vorticity in the vortex centers.

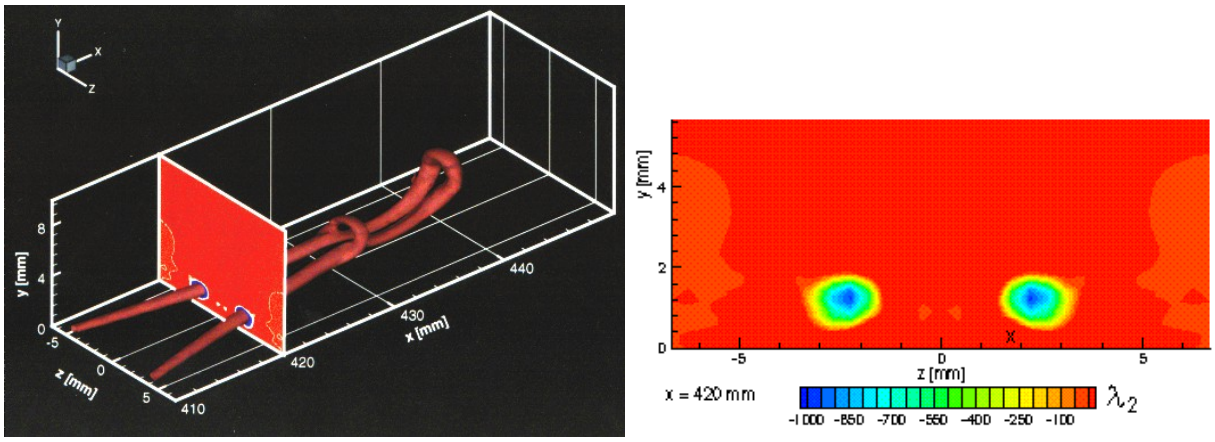

Figure 6. Vortex identification using the λ_2 method. Left: definition of the cutting plane at $x = const.$ Right: contours of λ_2.

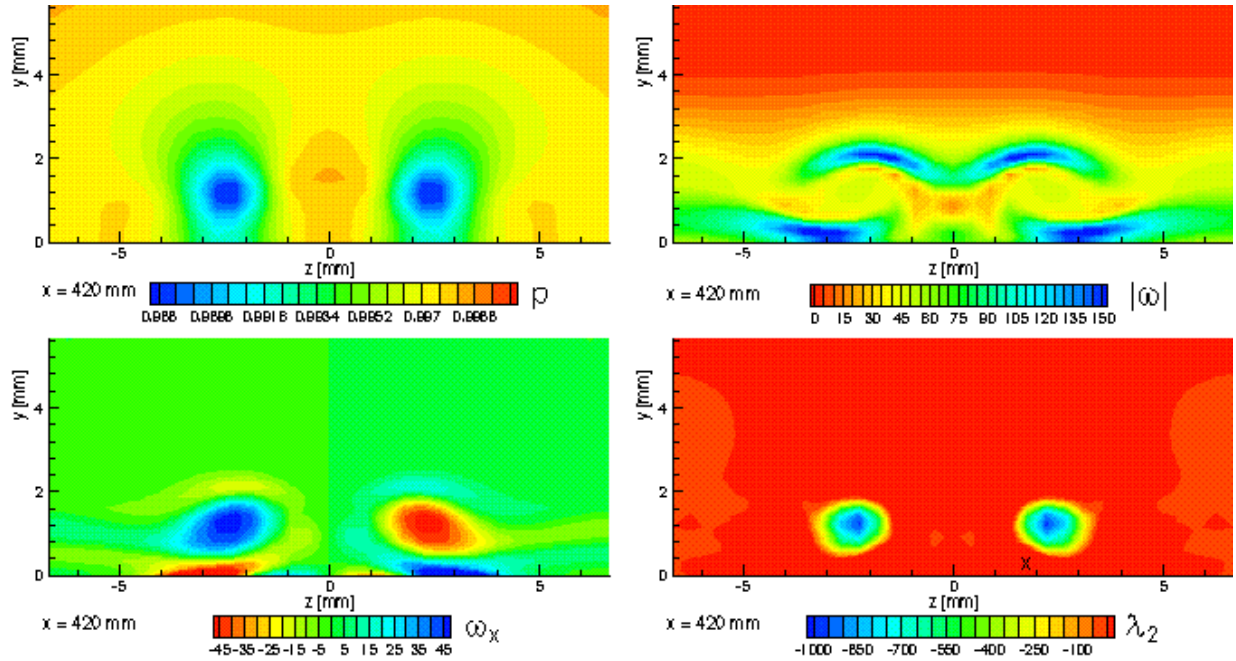

Figure 7. Comparison of pressure *p*, vorticity magnitude $|\omega|$, streamwise vorticity ω_x, and λ_2 in a cutting plane at *x = 420 mm.*

Comparisons along wall-normal cuts are performed in Figure 8. The curves are again scaled such that their shapes can be easily compared. New is the inclusion of streamwise vorticity here. The local pressure minimum agrees with the λ_2 minimum (note the inverted scales). The vortex is embedded in a region of wall-normal pressure gradient such that finding and choosing a meaningful threshold for vortex identification becomes difficult. As before, $\lambda_2 = 0$ selects the inflection points of the pressure field to define the extent of the vortex, i.e. $p \neq const.$ because of the pressure gradient. The streamwise vorticity confirms the presence of the vortex with shear layers on either side as observed above. Such an excellent agreement adds to the credibility of the λ_2-method. The comparison with the magnitude of the imaginary part λ_{ci} of the complex eigenvalues is as excellent as with the streamwise vorticity. Between $y \approx 2.4$ and $y = 4.0$ there is a second area where complex eigenvalues occur indicating that a vortical motion is possible according to Chong *et al.*[7]. However, this must be classified as a "spurious vortex" since no other criterion confirms the presence of a vortex there. A similar case is also presented in Jeong & Hussain[14]. Comparing λ_2 with the imaginary part of the eigenvalues one may say that the presence of imaginary eigenvalues of the velocity-gradient tensor is a necessary but not a sufficient condition for the presence of a vortex. Overall the λ_2-method appears reliable and robust compared to other methods (more examples can be found in Ref. 14). Another observation is that stronger vortices have stronger λ_2 extremes than weaker ones, in agreement with pressure, swirling strength, and vorticity.

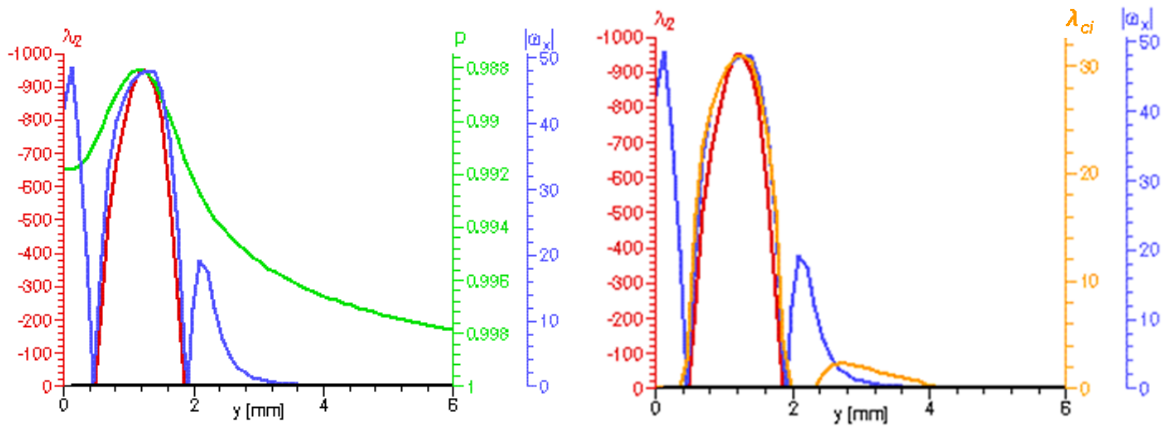

Figure 8. Comparison of the scalar vortex identification criterion λ_2 with streamwise vorticity magnitude $|\omega_x|$ and pressure p (left), and with the magnitude of the imaginary part of the eigenvectors of the velocity-gradient tensor λ_{ci} and streamwise vorticity magnitude $|\omega_x|$ (right).

C. Segmentation of Vortices

The λ_2-method is now applied to the DNS data set of Bake *et al.*[2]. A snapshot of a data section starting somewhat farther downstream than Figure 1 is presented as an overview in Figure 9.

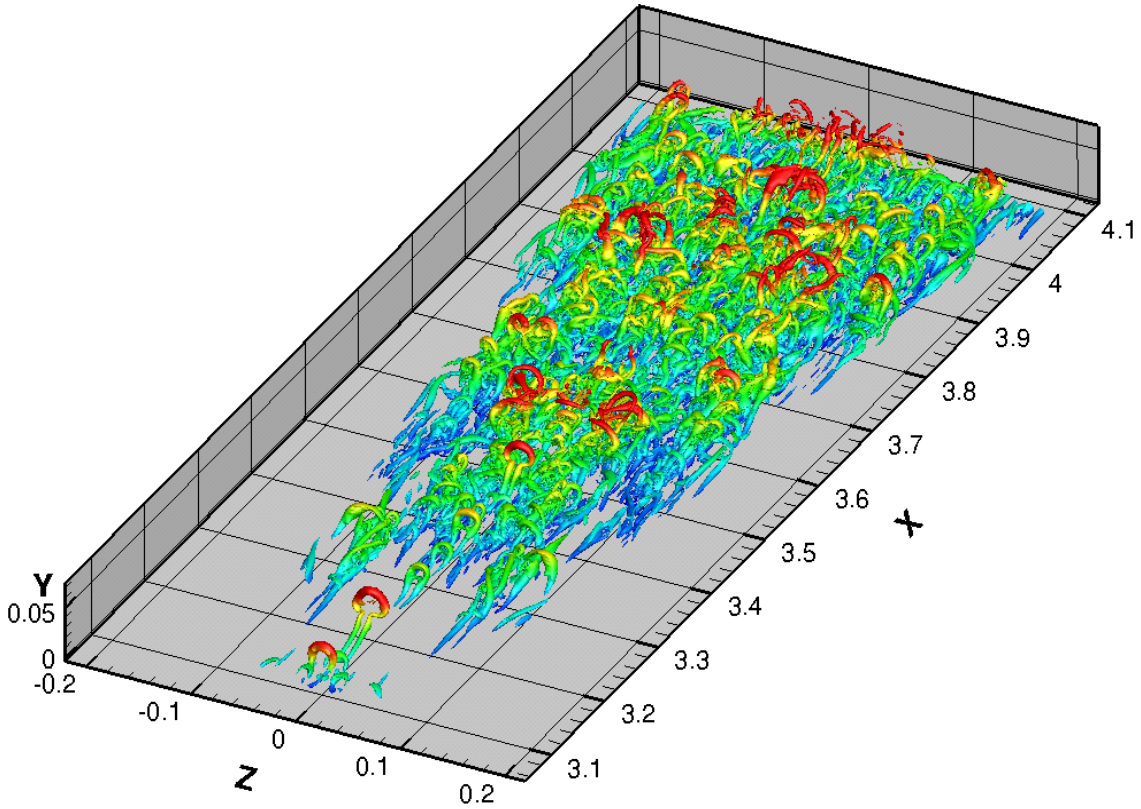

Figure 9. Vortices identified by $\lambda_2 = const.$ Color depicts wall distance.

Reducing the visualization to vortices yields a picture that is richer and clearer because visual occlusions by the boundary-layer shear are eliminated. Thus, the visualization depicts a snapshot of the unsteady transitional structures which form a turbulent wedge starting from the hairpins observable at $Z = 0$ and $X < 3.2$. Trains of hairpins are visible until $X \approx 3.5$ but only in the central part. Off center, close to the wall, and at the spanwise edges of the wedge longitudinal vortices dominate. Getting entangled with each other they develop asymmetric or one-sided loops at

their upper sides. Spanwise symmetry is broken after $X \approx 3.6$ due to the rapid growth of asymmetric background disturbances. The latter have been intentionally introduced[27], because otherwise the spanwise symmetry would remain forever.

The validations in the previous section have shown that the magnitude of λ_2 inside a vortex is proportional to the magnitudes of vorticity and swirling strength. This means that stronger vortices contain lower λ_2 compared to weaker ones. Changing the threshold for computation of λ_2 iso-surfaces must then allow to include weaker vortices if the threshold value is raised or to concentrate on stronger vortices if the threshold is decreased. Unfortunately, the outcome of such an operation is only partly successful as can be seen in Figure 10, because the effect of lowering the λ_2 threshold is two-fold. Weaker structures are lost as expected, but the stronger structures become thinner at the same time, i.e. information is lost. On the other hand, if λ_2 is raised towards zero the view on individual structures becomes obstructed and visual clutter increases.

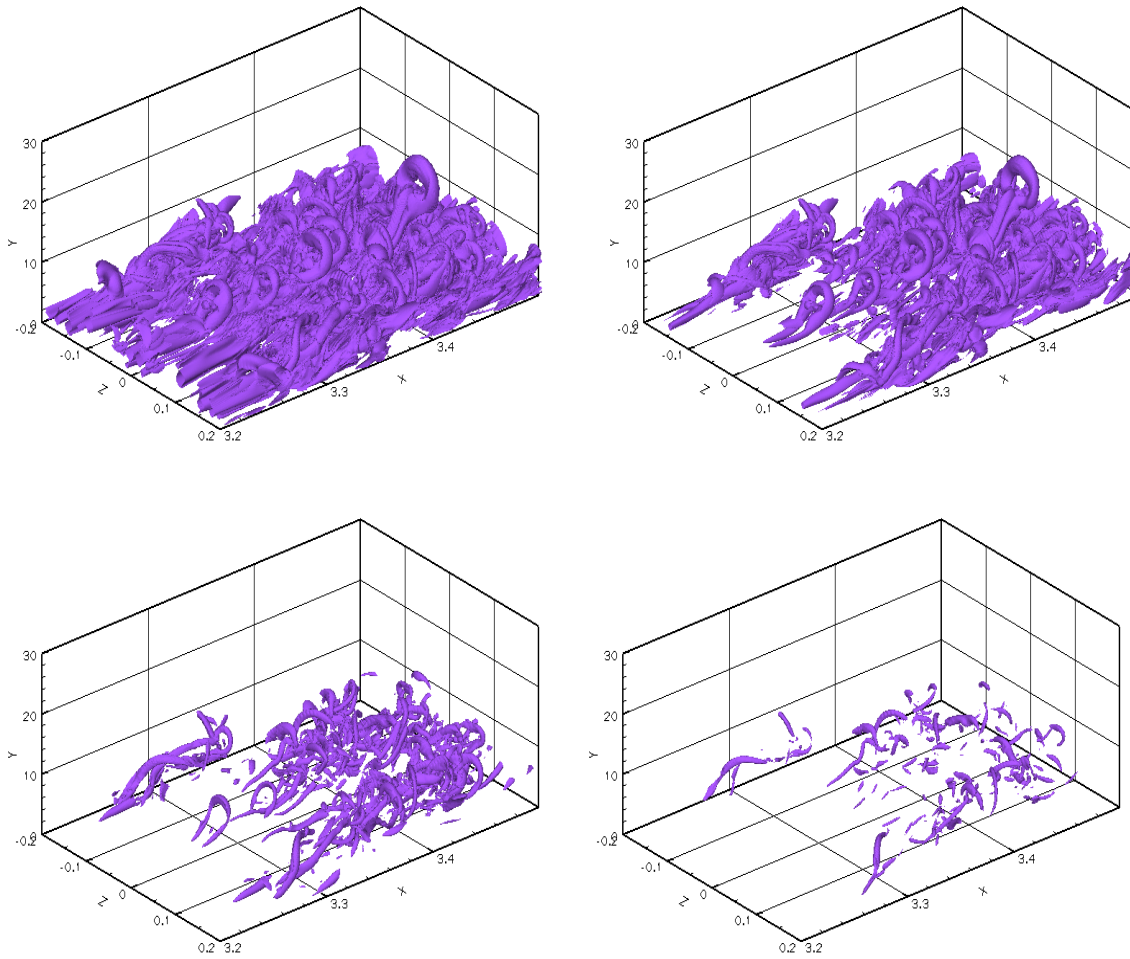

Figure 10. Effect of λ_2 threshold on vortex visualization (λ_2 = -1, -10, -80, and -320, top left, top right, lower left, and lower right, resp.). The number and size of the visualized structures depends on the chosen threshold.

To reduce these effects without losing information we followed the work of Samtaney *et al.*[31] and used a region-growing algorithm that starts from the global λ_2-minimum in the data set extracting all connected data points into a new data structure until a given threshold is encountered. After this the remaining data are searched for the next λ_2-minimum and the procedure is repeated until all structures have been extracted. Using such segmented vortices, visualizations of single snapshots can be greatly enhanced, see Figure 11. Each vortex segment can be assigned a different color and the user can select which structures he would like to see. This reduces visual occlusions when necessary and allows concentrating on selected structures. However, as the flow evolves, when more and more

vortices appear, several of these are no longer separated by high-enough λ_2 values and they agglomerate to lumps of vortices, see the large green and red structures at the foremost right boundary in Figure 11.

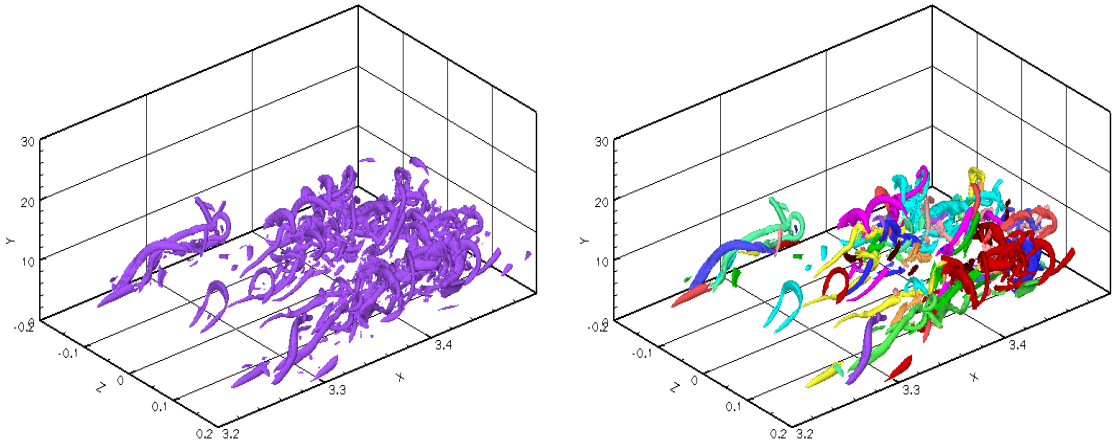

Figure 11. Result of segmentation of the vortex field showing the 160 most intensive structures for the threshold λ_2 = -80.

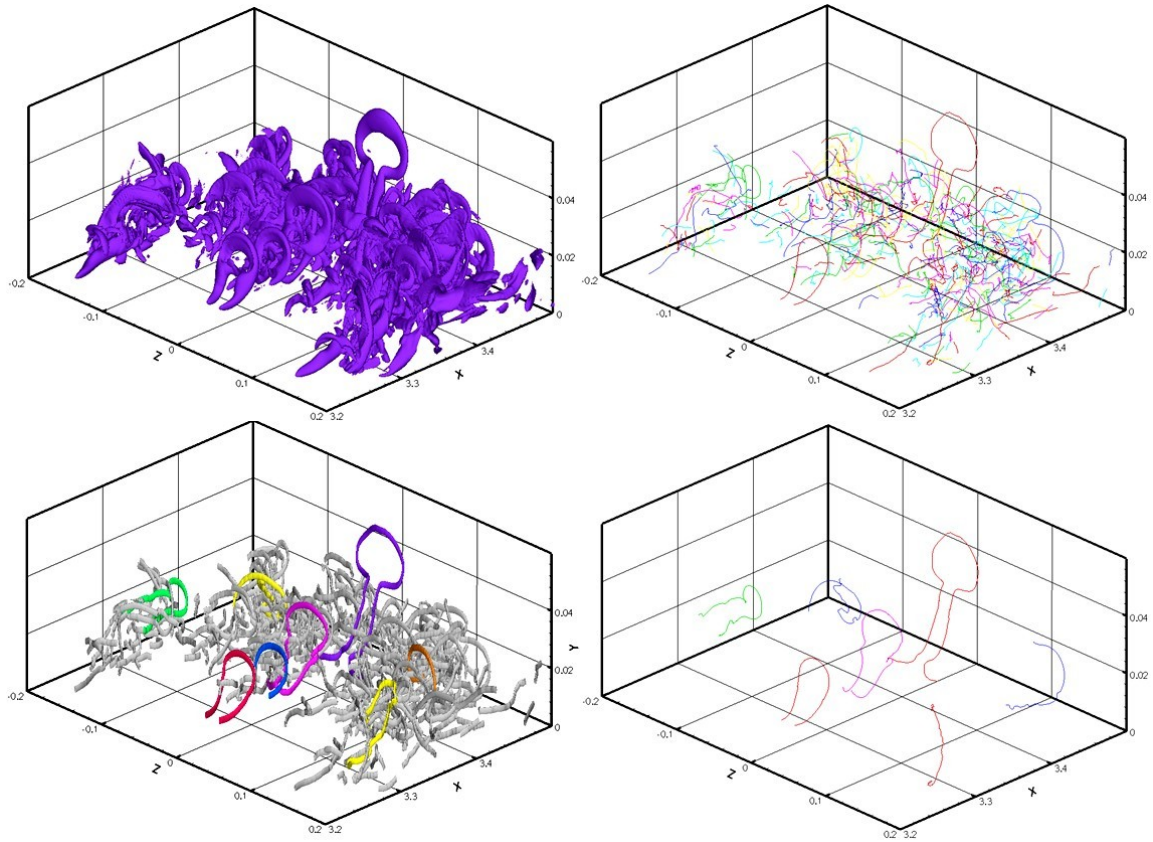

Figure 12. Examples for the extraction of vortex axes from the scalar field $\lambda_2(x, y, z)$. Upper left: iso-surface λ_2 = *const.* Upper right: lines connecting local λ_2 minima. Lower left: enhanced visualization using a finite core radius and color to put selected vortices in focus. Lower right: isolation of selected vortex axes.

To avoid the problems shown in Figure 10 Linnick & Rist[23] have suggested extracting λ_2 extrema-lines from the data (i.e. lines connecting the local minima). It has been checked that these faithfully represent vortex axes. A

sample output is illustrated in Figure 12. The picture in the upper left corner repeats the above observations that iso-surfaces of $\lambda_2 = const.$ contain a lot of visual obstructions if too many vortices are present. In addition, individual vortices are hard to recognize when all iso surfaces use the same color. Reducing all vortices to their λ_2 minima and using different colors for different lines helps to depict the individual vortices without occlusions (next subfigure). However, the spatial structure is lost due to projection of the three-dimensional space on two dimensions. The number of vortices may also be too large for fast perception, interpretation and understanding of the picture. A simple but effective enhancement is shown in the lower left corner of the figure. For this the vortex axes are drawn with a constant, finite, user-defined diameter. This allows using color, lighting and shading in order to make the perception of the three-dimensional structure of the lines possible. Showing selected vortices in color together with the others in gray leads to a so-called "focus-and-context" visualization where each structure can be viewed in context to the others. For the study of single structures (without occlusions by the others) these can also be viewed in isolation, as shown on the lower right image.

D. Vortex Tracking

Since we deal with unsteady structures here, the next step is to track vortices in time. Since we perform the vortex segmentation on snapshots of the flow field, this means that we must find corresponding structures in two subsequent snapshots using a tracking algorithm that compares spatial positions and some meaningful criteria like size or strength of the candidates. Here, our decision to use vortex axes has an immediate advantage. It suffices to extract the local velocity vector on a point on the axis to know the convection speed of the vortex at that point. Using this, it is straightforward to estimate its position in the next snapshot and compare this estimation with the candidate vortices. This reduces the number of candidate vortices considerably. For estimation we use Heun's method which is a second-order accurate predictor-corrector scheme that estimates new positions using the average between the velocities at the old time step and those predicted by an explicit first-order predictor step. Corresponding vortices are identified if the point-to-point distance along two vortex axes is minimal and below a user-defined threshold.

The initial position of three vortices, the prediction of their new position and their comparison with the corresponding vortices at the new time step are illustrated in a top view on the boundary layer in Figure 13. The agreement between estimation and real position is excellent in light of the large distance between the two time instants which is 80 times the computational time step used to solve the Navier-Stokes equations here.

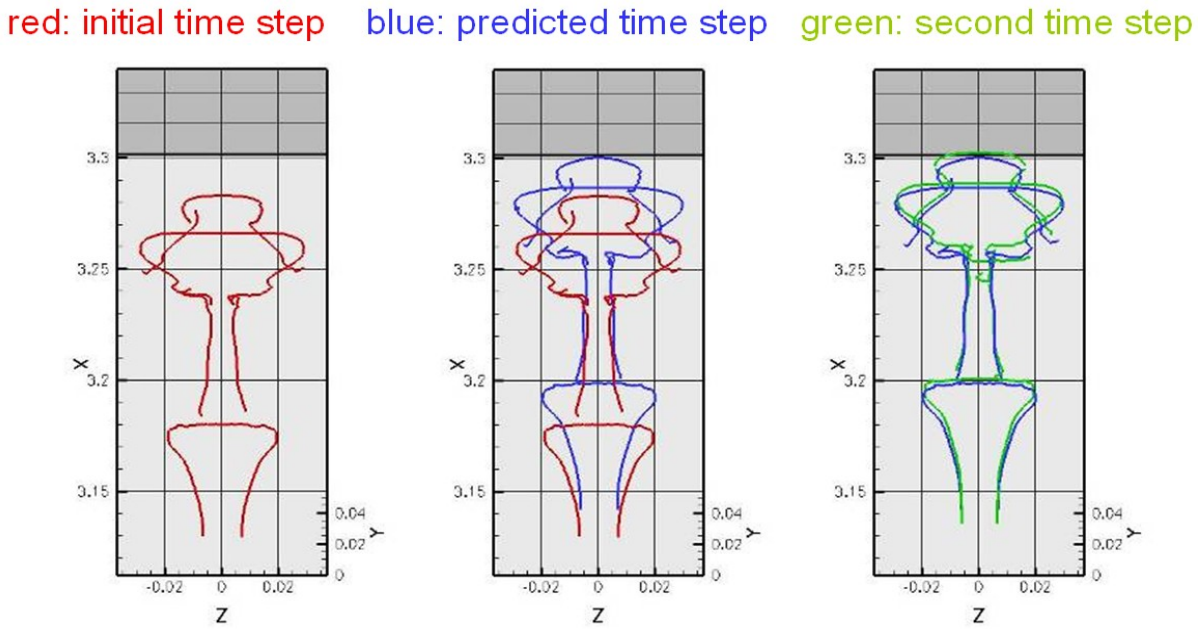

Figure 13. Illustration of vortex-line tracking in time using a predictor-corrector scheme.

Figure 14 presents an example of automatic tracking of vortices during the process of Ω-shaped hairpin vortex formation already sketched in Figure 2 further above. The symbol t_p is used to designate the normalized phase of each snapshot with respect to the forcing of the 2D Tollmien-Schlichting waves at the disturbance strip. As such, t_p = 0.5, and 1.0 correspond to phase angles of π and 2π, respectively.

The present visualization is a combination of λ_2 iso surfaces and extracted vortex cores. Colors (red, blue, orange) once assigned at the first occurrence of a core line to a particular line are retained assigned to the same vortex throughout the whole sequence such that individual vortices can be visually followed.

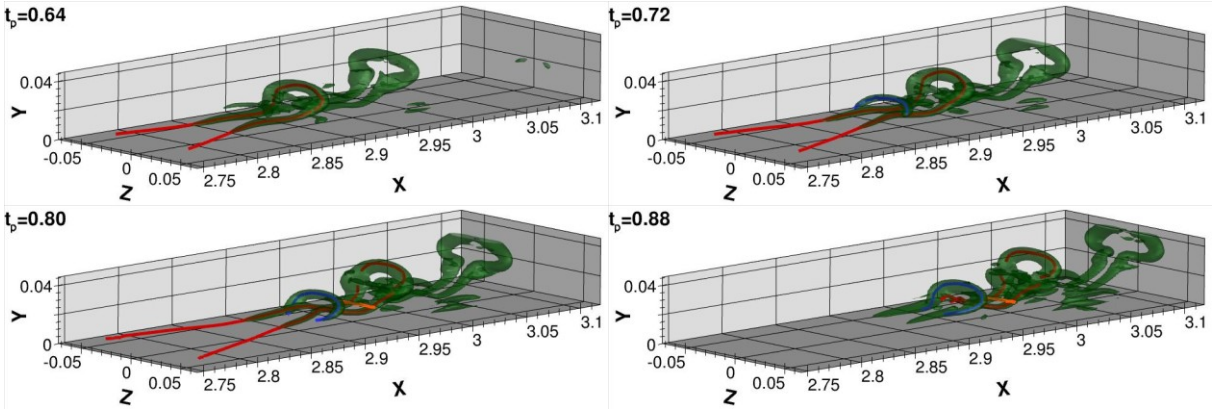

Figure 14. Tracking of vortices using core lines and iso-contours λ_2 = *const.* Color is used to identify the same vortex segment in each plot (and in the following figures).

Figure 15 presents a side and a top view on two tracked vortices from Figure 14. Only the lines (vortex axes) are shown. The structures move and develop from left to right as time evolves. The red structure appears five times, i.e. once in each snapshot. But the blue vortex appears only four times because it emerges first in the second snapshot where it starts as a (blue) "bridge" between the (red) "legs" of the Λ. Later on it evolves into a new Ω-vortex (blue). When the most downstream Ω (red) is torn away from the rest in the last two snapshots the blue Ω becomes the new head of the remaining Λ and the latter turns blue.

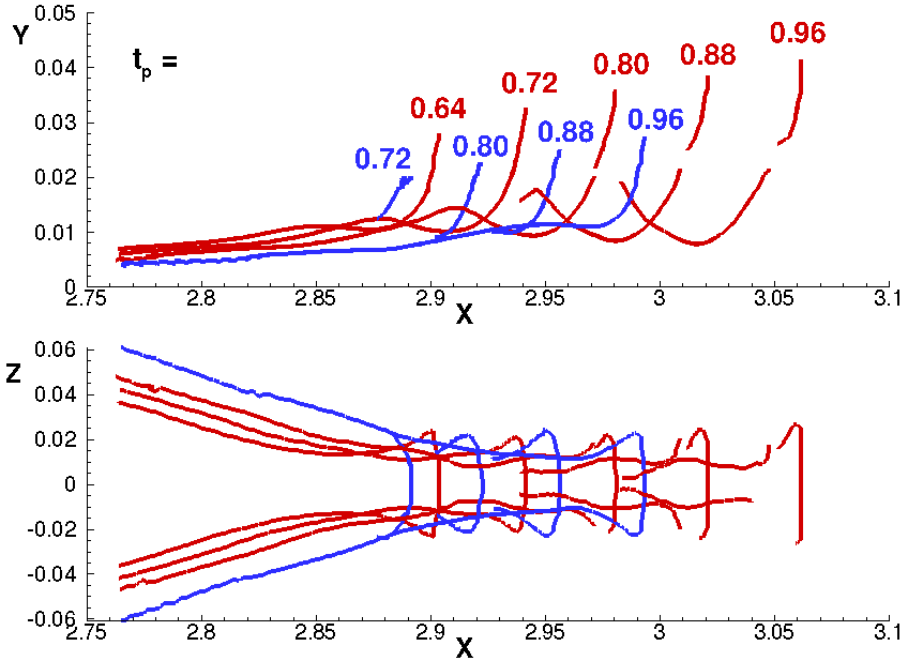

Figure 15. Tracking of selected vortices. Side and top views on the extracted vortex cores, cf. Figure 14. t_p = normalized time (phase) with respect to disturbance period.

E. Feature Extraction along Vortex Axes

Once the tools to automatically extract and track vortices in time exist, the next step consists of quantifying the phenomena. The underlying idea is that this may help to get "insight" and to "understand" the flow, e.g. by building simpler, mental or mathematical models. In the context of vortices, people usually think of particle (vortex) methods which describe the flow field in a Lagrangian frame[22]. The idea of reducing flow-field data to vortices and

quantifying these is not new. Fernandez *et al.*[10] have suggested the term "visiometrics" for quantifying visual objects in their pioneering work.

It is straightforward to combine the vortex-axes extraction of the previous sections with an extraction of other scalar or vector data along the line. Extracted velocity vectors have already been used in the previous section for the temporal tracking. In the present data sets we have extracted several quantities along the vortex axes, like circulation, vorticity, super helicity density, enstrophy production rate, and energy dissipation rate. Some of these were not useful to gain additional insight, others were partly useful. Overall, there is no real breakthrough so-far. The problem itself seems ill-posed. It is very difficult to define what we mean be "insight" and how to get it or how to quantify physical phenomena, like the birth of a new vortex or the interactions between two vortices. Feature extraction applied to the present data sets offers some additional information, but an immediate better understanding of the observations does not follow by itself.

An example for tracking of λ_2 and the enstrophy production rate is presented in Figure 16. The latter quantity is defined as

$$P = \boldsymbol{\omega}\, \mathbf{S}\, \boldsymbol{\omega}, \tag{2}$$

where $\boldsymbol{\omega}$ is the vorticity vector, and $\boldsymbol{S}$ the strain-rate tensor, see Ref. 17.

Presenting two quantities in one figure allows detailed comparisons of the two. For the physical shapes of the selected vortices Figure 15 and Figure 2 should be consulted again. The colors are still the same as before. In the top part of Figure 16 we show the development of the strength of the two selected Ω-vortices. At t_p=*0.64* the most intensive rotation (λ_2 minimum) is at the downstream tip of the first Ω. At the same time there is a negative enstrophy-production rate at the same position. Positive *P* appears further upstream at the lower end of the Ω-loop where a second λ_2 minimum appears. Following the red structure over time one observes that the rotation increases at the lower end of the Ω-loop while it decreases at its upper (most downstream) end. The interesting observation is that increase and decrease of vortex strength correlates well with positive and negative enstrophy production. The same holds for the second Ω-vortex shown in blue color. This vortex starts out as a "bridge" between the "legs" of the primary Λ at t_p=*0.72*. The λ_2 minimum at its downstream end (i.e. again at the highest point of the newly formed Ω) increases over time. Towards the end at t_p=*0.96* the maximal enstrophy production moves to the rearward, lower end of the loop and a second λ_2 minimum starts to develop there. Thus, the process of vortex-loop generation repeats.

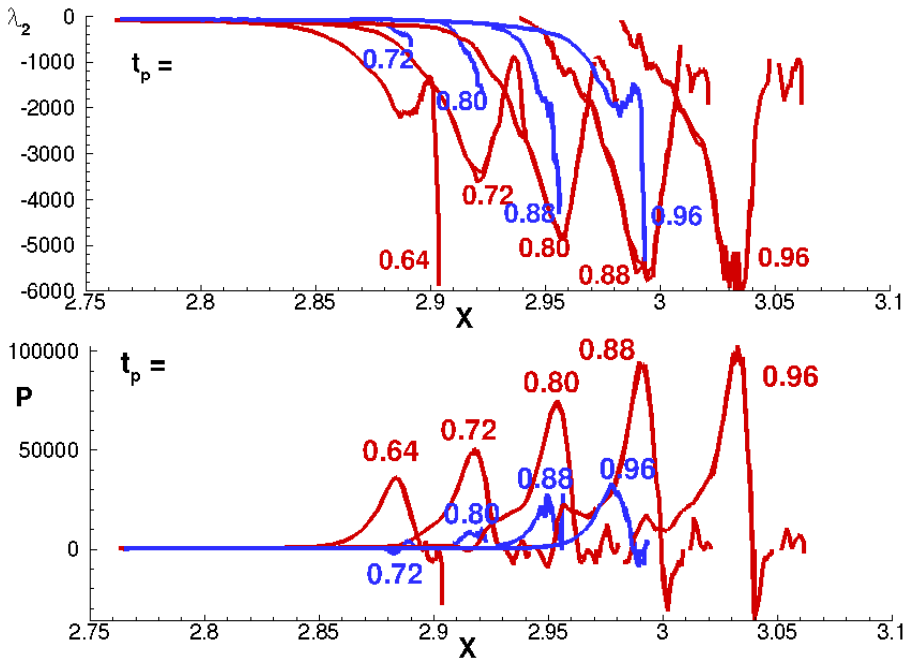

Figure 16. Tracking of λ_2 (top) and enstrophy-production rate *P* (bottom) for the vortices shown in the previous figures (color is used to identify the same vortices in each figure).

In Figure 17 we follow one hairpin vortex for a longer time and compare its shape in a side view (top figure) with its strength, expressed by λ_2 (middle), with the enstrophy-production rate P (lower figure). Color is used to identify and relate the different snapshots in each of the three plots to each other.

In the first four snapshots λ_2 at the downstream tip of the vortex decreases in accordance with the enstrophy-production rate which is maximal at the tip during the first three time steps. At the fourth time step enstrophy-production rate at the tip crosses zero and afterwards it turns negative for another six time steps. λ_2 increases indicating decreasing swirling strength at the downstream tip of the vortex (top of an Ω-loop). Starting with the fourth time step a new P maximum develops at the lower end of the Ω-loop. Again in agreement with this, the strength of the vortex increases there such that a new λ_2 minimum develops after the sixth time step.

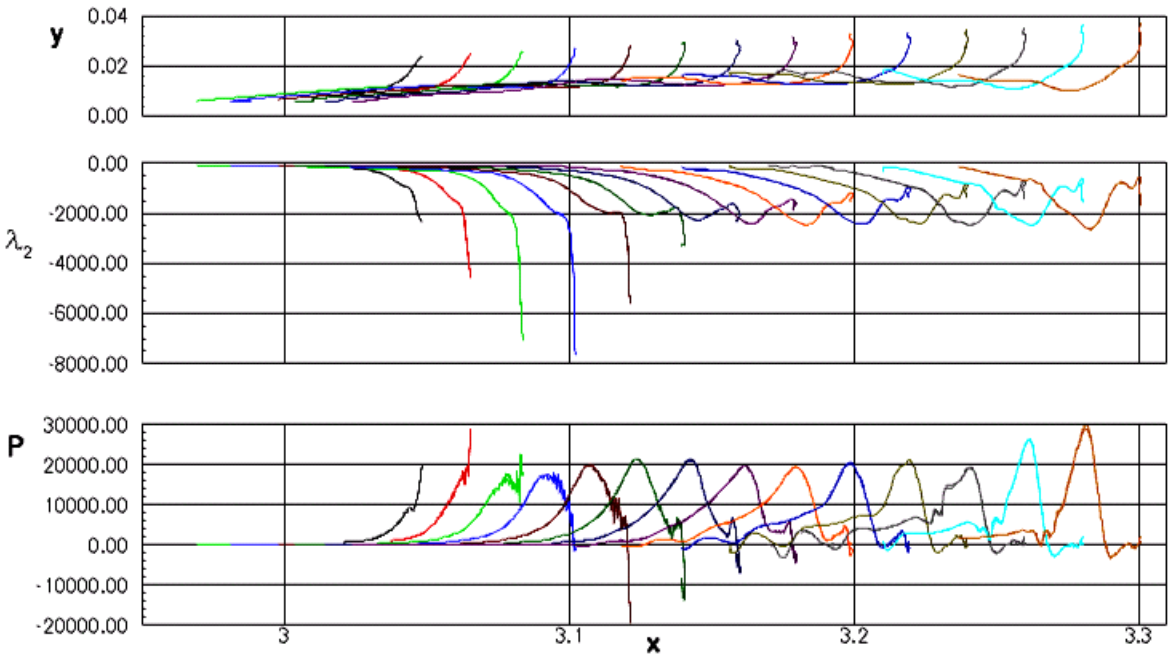

Figure 17. Spatio-temporal evolution of a selected hairpin vortex. Top to bottom: side view (y vs. x), "vortex strength" λ_2, enstrophy production rate P. Here, color is only used to distinguish the different time instants.

These observations indicate that data extracted from snapshots can not only be used to confirm, predict or quantify the present state of the flow but also contribute to a better understanding of its temporal evolution. This is exactly what we meant by "insight" or "understanding" further above. However, the problem is difficult and far from being solved.

Another example is tracking of the energy dissipation rate, defined as

$$E_{dis} = \frac{1}{2}\left(\frac{\partial u_j}{\partial x_k} + \frac{\partial u_k}{\partial x_j}\right)^2, \tag{3}$$

where u_j, u_k are the velocity components in x_j and x_k direction, respectively, see Ref. 18. Einstein's summation convention is used for the indices. Tracking of E_{dis} is shown in Figure 18. It reveals that the maxima of this quantity occur in the topmost parts of the Ω-loops which are farthest away from the wall. Especially the new vortex (blue) dominates over the "old "one (red). The reason for this is that E_{dis} correlates with shear and that the far-away parts of the vortices are embedded in streamwise shear (spanwise vorticity), cf. Figure 4 right.

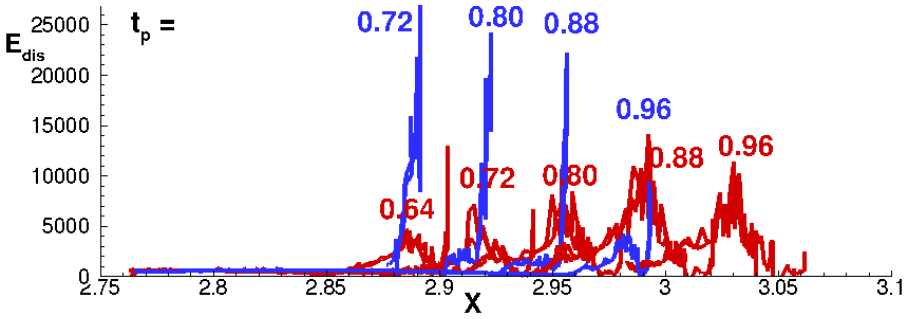

Figure 18. Tracking of energy dissipation rate E_{dis} for the vortices shown in the previous figures (color is used to identify the same vortices in each figure).

Integrating the vorticity identified as belonging to vortices it is possible to compute an induced velocity field using the Biot-Savart law. This information can then be used to study the mutual interactions of the vortices. Figure 19 presents induced velocity magnitude on the iso-surfaces $\lambda_2 = const.$ depicting vortices. The most active areas are the Ω-loops and the small streamwise tails under them.

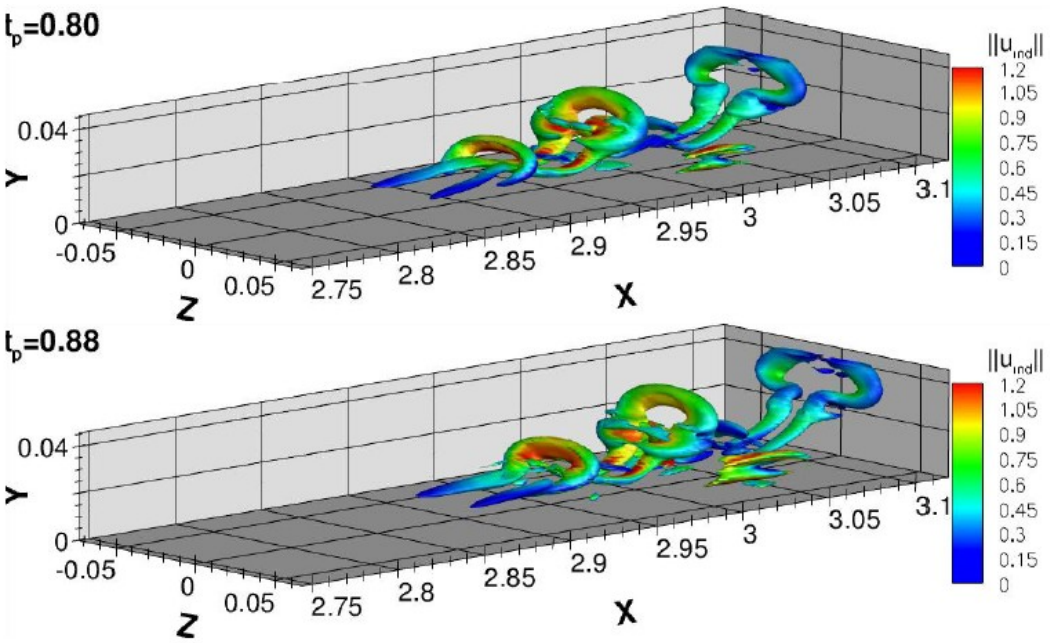

Figure 19. Visualization of induced velocity magnitude on the iso surfaces λ_2 = const. at two time instants.

Using the induced velocity, induced enstrophy and induced kinetic energy have been computed as well. Figure 20 shows a comparison of iso-surfaces of induced enstrophy (red) and iso-surfaces of λ_2 (green). This is very instructive: Pronounced induced enstrophy maxima occur inside the top of the Ω-loops and inside the streamwise "legs" of the hairpins, precisely at those positions where the latter are closest to the wall. The according observations in the previous figures can thus be identified as an effect of self-induction of the vortices. This is another example that shows that identification and quantification of observations leads to additional insight.

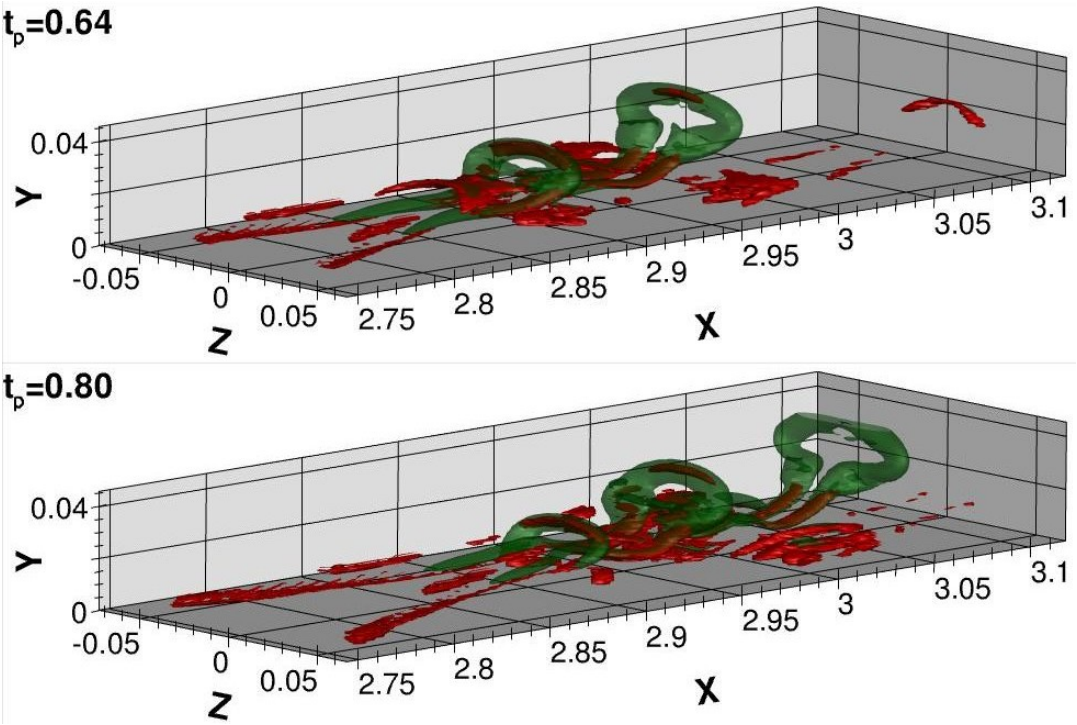

Figure 20. Comparison of iso surfaces of induced enstrophy (red) with λ_2 iso surfaces (vortices).

IV. Inclusion of Shear Layers

Since vortices in a viscous flow contain and produce shear and because new vortices can be generated out of shear it is necessary to consider shear layers in addition to vortices. In Refs. 23, 26, and 32 we have proposed a method similar to the λ_2-method of Jeong & Hussain[14] for shear layer identification.

$$I_2 = \frac{1}{2}(S_{ii}S_{jj} - S_{ij}S_{ij}), \tag{4}$$

where I_2 is the second invariant of the shear stress tensor $\boldsymbol{S}$, and S_{ii}, and S_{ij} denote its diagonal, and off-diagonal elements, respectively, again using Einstein's summation convention. This quantity can be computed and used for shear-layer visualization ($I_2 < 0$) in the same way as the quantity λ_2 for vortex visualization. Compared to the method proposed by Haimes & Kenwright[11] it is faster to compute because no eigenvalues must be calculated. The relation between the two is

$$S_{HK} \sim \sqrt{-I_2}, \tag{5}$$

where stands for the scalar suggested by Haimes & Kenwright.

Using both methods together yields additional insight, see Figure 21 and the annotations given in the figure. The vorticity is now split into two parts, one depicting pure shear, and the other vortex-related vorticity. An interesting impression, especially for the late-stage transition depicted in Figure 22 is that initially the vortices are completely embedded in the boundary layer, where all of them originate. In the further development, starting around the spanwise peak station, vortices move farther away from the wall and thus into a low-shear region that is no longer depicted by the chosen I_2 threshold. This is why the view on the later-stage vortices is no longer obstructed by the chosen shear level. Overall Figure 22 can be compared with the visualization of the vortices alone in Figure 9 because both show the same data.

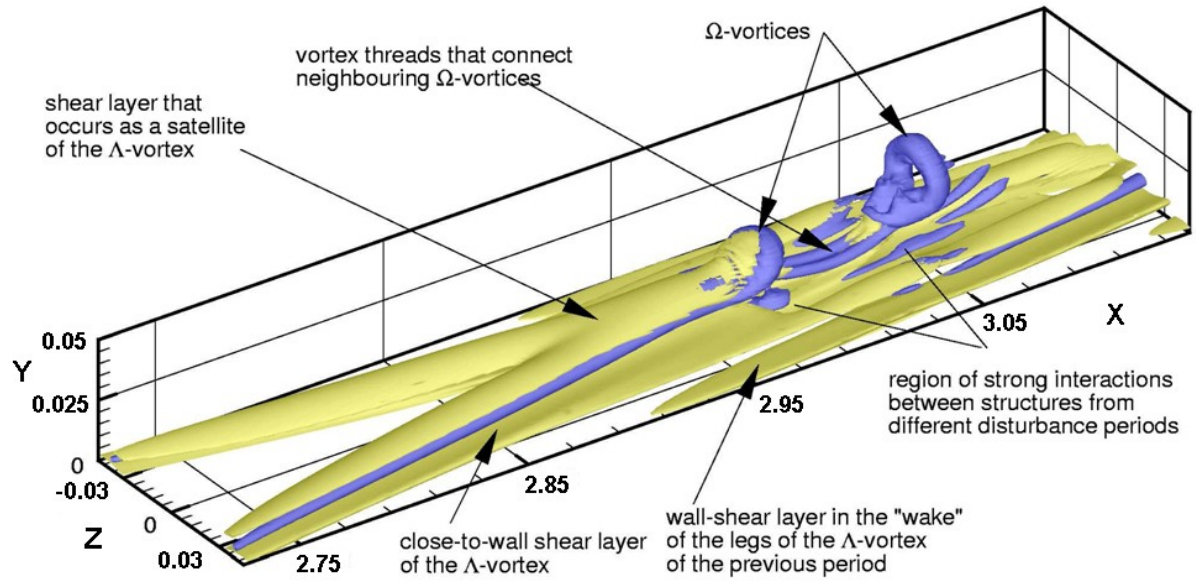

Figure 21. Comparison of areas of high shear depicted by $I_2 = const.$ (yellow) with vortices identified by $\lambda_2 = const.$ (blue).

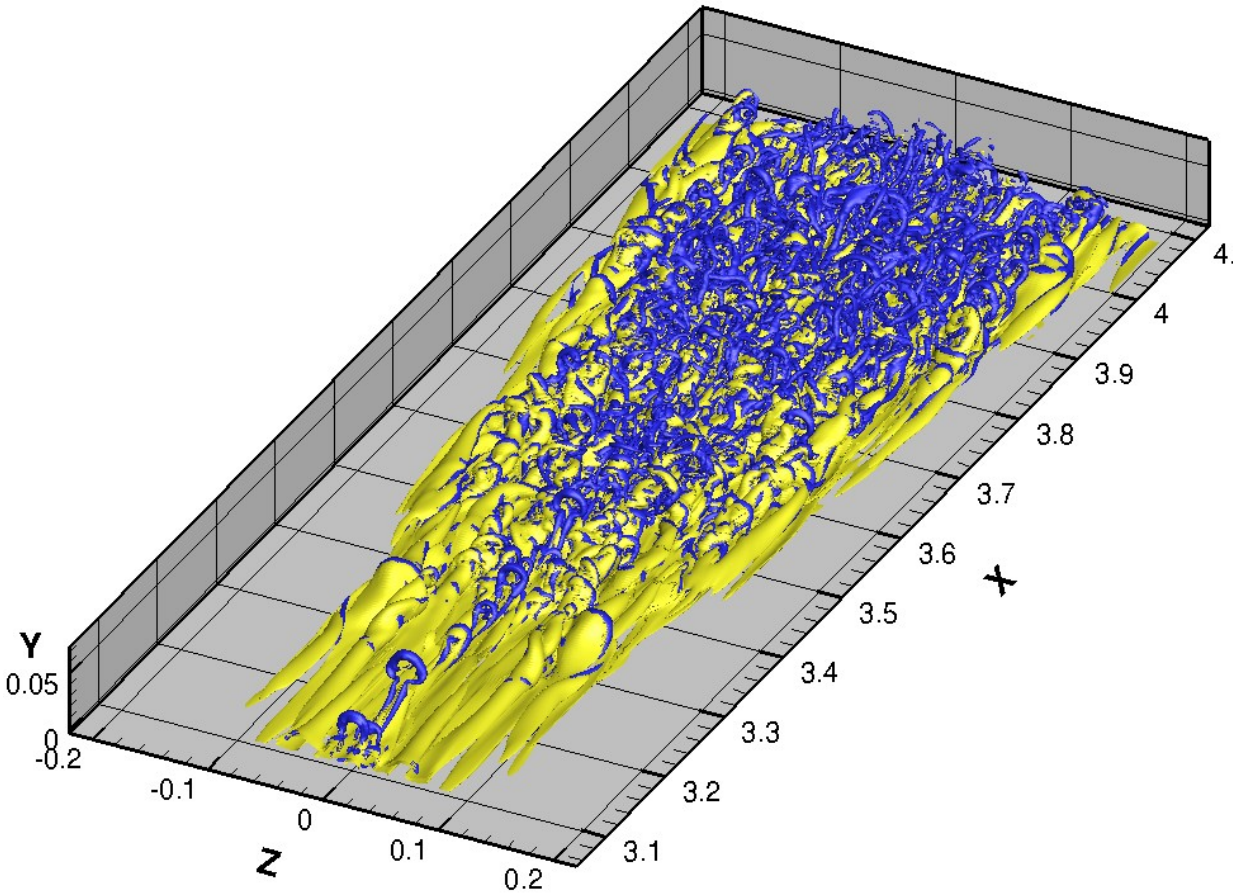

Figure 22. Comparison of high shear depicted by $I_2 = const.$ (yellow) with vortices identified by $\lambda_2 = const.$ (blue) for the late-stage laminar-turbulent transition.

V. Outlook and Summary

A problem of the λ_2-method has been identified by Wu *et al.*[36] The trouble occurs when a vortex is subjected to axial strain. By means of test data Wu *et al.* show that using λ_2 in such a case leads to smaller vortices than expected. For correction they propose a variant of the Q-method which they call Q_{2D}, see Ref. 36. So far, we are not aware of any publication that confirms Wu *et al.* for DNS data. This is why we try this here.

The circles in the top row of Figure 23 indicate two positions where the cut vortex is of crescent shape instead of a more common (or expected) elliptical shape. Comparing the contours of λ_2 (color) with the position of high-shear layers (black contour lines) shows that the two suspect vortices lie in an area of high shear that leads to axial stretching. The missing part in the λ_2-method exactly follows an I_2 contour line. As the more intensive vortex pair in the center of the figure also touches the shear layer, the concave part in the outline of the central vortex pair could also be due to axial stretching. In fact, using the Q_{2D}-method of Wu *et al.*[36], shown in the lower part of the figure, confirms these interpretations as all suspicious vortices appear now more complete without the previous crescent shape outlines or concave contour lines when viewed from the outside.

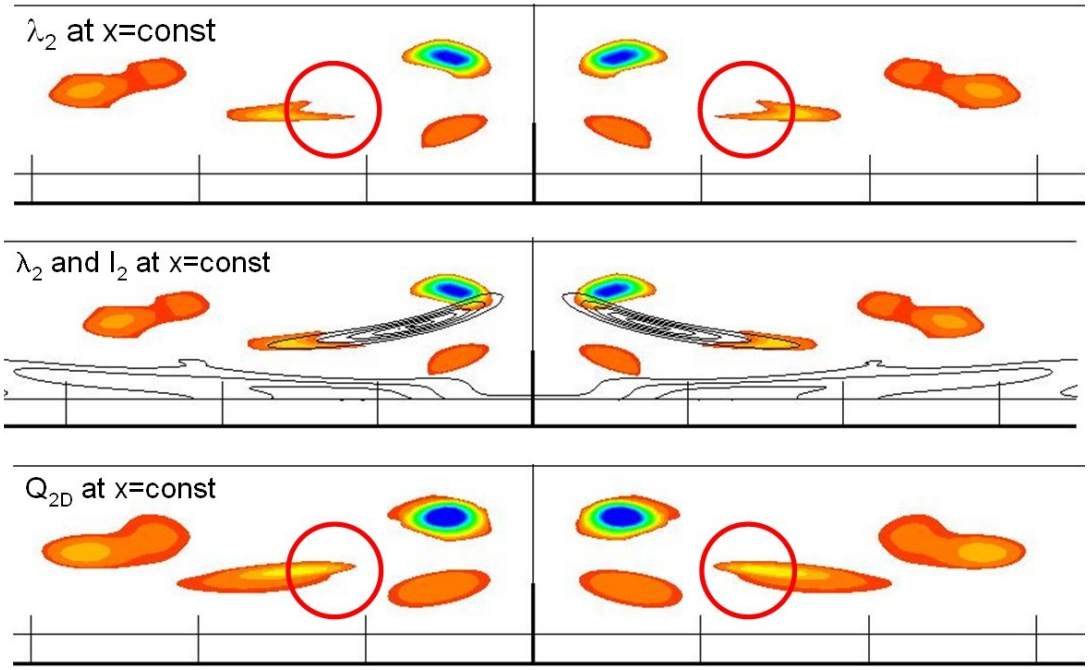

Figure 23: Comparison of vortex identification methods at *X=3.15* using contours of λ_2, I_2, and Q_{2D}.

In principle, all analyses presented above which are based on the λ_2-method could be repeated using the Q_{2D}-method, even if the computing time would be considerably larger because of the need to search for the best 2D base-reference system[21,36]. However, the overall difference between using the Q_{2D}-method instead of the λ_2-method is rather subtle, as can be judged from comparing two iso surfaces for the same data in Figure 24 such that this change in paradigm is not mandatory.

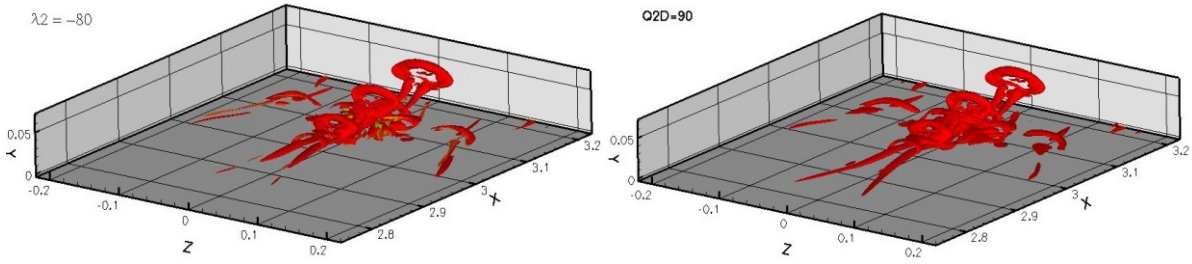

Figure 24. Comparison of iso surfaces $\lambda_2 = const$ and $Q_{2D} = const$.

Summarizing the present work, the following statements are appropriate. Yes, it is possible to get additional insight into the mechanics of a transitional boundary layer using enhanced visualization tools. Some snapshot examples have been presented here. Descriptions of two software systems for *interactive* exploration of the data which have been created in cooperation with the visualization and interactive systems group at the University of Stuttgart can be found in Refs. 32 and 33. There, the concept of induced enstrophy and energy has proven helpful for selecting the most active or "interesting" features of the flow. The next necessary steps are the search for criteria to detect and quantify mechanisms like the generation of vortices out of shear layers and the different basic interactions among vortices. Such information is necessary to decompose the complicated gearbox shown in Figure 22 into its basic elements which the present author deems important for understanding late-stage laminar-turbulent transition or turbulence. Work on generic cases like breakdown of a 2D shear layer where the generation of vortices and the pairing of two vortices are present has been started recently[3,4]. With respect to vortex-vortex interactions the literature is full of examples, e.g. 16, 17, 18, 25, etc. We first need a literature survey in order to check whether newer methods like those presented here have a chance to yield additional insight that can be incorporated into a software tool that helps to decompose the transitional or turbulent flow field into its building blocks. There is still much more to do than has been presented here.

Acknowledgments

The author thanks his former students and assistants Kudret Baysal and Mark Linnick for their valuable research work on which the present article is based. The underlying DNS data are from Daniel Hug (nee Meyer). Computer time and long-time data storage provided by the German High-Performance Computing Center Stuttgart is highly acknowledged as well.

References

1. Adrian, R. J., "Hairpin vortex organization in wall turbulence," *Physics of Fluids*, Vol. 19, No. 4, 041301 (2007); doi: 10.1063/1.2717527
2. Bake, S., Meyer, D. G. W., and Rist, U., "Turbulence mechanism in Klebanoff-transition. A quantitative comparison of experiment and direct numerical simulation," *J. Fluid Mech.,* Vol. 459, 2002, pp. 217-243.
3. Baysal, K., „Untersuchungen zur Identifikation und Verfolgung von Strömungsfeldstrukturen," Dissertation Universität Stuttgart, 2011.
4. Baysal, K., and Rist, U., "Identification and quantification of shear layer influences on the generation of vortex structures," *New Results in Numerical and Experimental Fluid Dynamics VII*, Contributions to the 16. STAB/DGLR-Symposium, Aachen, Nov. 2008, edited by A. Dillmann, G. Heller, M. Klaas, H.P. Kreplin, W. Nitsche, W. Schröder, Notes on Numerical Fluid Mechanics, Vol. 112, Springer, 2010, 241-248.
5. Berdahl, C. H., and Thompson, D. S., "Eduction of swirling structure using the velocity gradient tensor," *AIAA Journal,* Vol. 31, No. 1, 1993, pp. 97-103.
6. Chakraborty, P., Balachandar, S., and Adrian, R.J., "On the relationships between local vortex identification schemes," *J. Fluid Mech.*, Vol. 535, 2005, pp.189-214.
7. Chong, M. S., Perry, A. E., and Cantwell, B. J., "A general classification of three-dimensional flow fields," *Physics of Fluids A*, Vol. 2, No. 5, May 1990, pp. 765-777.
8. Cucitore, R., Quadrio, M., and Baron, A., "On the effectiveness and limitations of local criteria for the identification of a vortex," *European Journal of Mechanics, B/Fluids*, Vol. 18, No. 2, 1999, pp. 261-282.
9. Falco, R. E., "New results, a review and synthesis of the mechanism of turbulence production in boundary layers and its modification," AIAA-1983-377, AIAA 21st Aerospace Sciences Meeting, Reno, NV, Jan 10-13, 1983.
10. Fernandez, V. M., Silver, D., and Zabusky N. J., "Visiometrics of complex physical processes: diagnosing vortex-dominated flows," *Computers in Physics*, Vol. 10, No. 5, Sept./Oct. 1996, 463-469.
11. Haimes, R., and Kenwright, D., "On the velocity gradient tensor and fluid feature extraction," AIAA Paper No. 99-3288, 14th Computational Fluid Dynamics Conference, Norfolk, VA, June 28-July 1, 1999.
12. Haller, G., "An objective definition of a vortex," *J. Fluid Mech*., Vol. 525, 2005, pp. 1-26.
13. Hama, F.R., and Nutant, J., "Detailed flow-field observations in the transition process in a thick boundary layer," Proceedings of the 1963 Heat Transfer and Fluid Mechanics Institute, Stanford University Press, Palo Alto, 1963, pp. 77-93.
14. Jeong, J., and Hussain, F., "On the identification of a vortex", *J. Fluid Mech.*. Vol. 285, 1995, pp. 69-94.
15. Kida, S., and Miura, H., "Identification and analysis of vortical structures," *European Journal of Mechanics B/Fluids,* Vol. 17, No. 4, 1998, pp. 471-488.
16. Kida, S., and Takaoka, M., "Bridging in vortex reconnection," *Physics of Fluids*, Vol. 30, Issue 10, October 1987, pp. 2911-2914.
17. Kida, S., and Takaoka, M., "Vortex reconnection," *Ann. Rev. Fluid Mech.*, Vol. 26, 1994, pp. 169-189.
18. Kida, S., Takaoka, M., and Hussain, F., "Collision of two vortex rings," *J. Fluid Mech.*, Vol. 230, 1991, pp. 583–646.

19. Klebanoff, P. S., Tidstrom, K. D., and Sargent, L. M., "The three-dimensional nature of boundary-layer instability," *J. Fluid Mech.*, Vol. 12, 1962, pp. 1-34.
20. Kloker, M. J., "A robust high-resolution split-type compact FD-scheme for spatial direct numerical simulation of boundary-layer transition," *Applied Scientific Research,* Vol. 59, No. 4, 1998, pp. 353-377.
21. Kolar ,V., "Vortex identification: New requirements and limitations," *International Journal of Heat and Fluid Flow*, Vol. 28, Issue 4, August 2007, pp. 638–652.
22. Leonard, A., "Computing three-dimensional incompressible flows with vortex elements," Ann. Rev. Fluid Mech., Vol. 17, 1985, 523-559.
23. Linnick, M., and Rist, U., "Vortex Identification and Extraction in a Boundary-Layer Flow," *Vision, Modeling, and Visualization 2005, Proc. November 16-18, 2005, Erlangen, Germany,* edited by G. Greiner, J. Hornegger, H. Niemann, M. Stamminger, Akad. Verlagsges. Aka, Berlin, pp. 9-16.
24. Lugt, H. J., "Vortex Flow in Nature and Technology," New York et al., John Wiley & Sons, 1983, 297 pages.
25. Melander, M. V., and Hussain, F., "Cross-linking of two antiparallel vortex tubes," *Physics of Fluids A*, Vol. 1, Issue 4, April 1989, pp. 633-636.
26. Meyer, D. G. W., „Direkte numerische Simulation nichtlinearer Transitionsmechanismen in der Strömungsgrenzschicht einer ebenen Platte," Dissertation Universität Stuttgart, 2003.
27. Meyer, D. G. W., Rist, U., and Wagner, S., "Direct numerical simulation of the development of asymmetric perturbations at very late stages of the transition process," *Recent Results in Laminar-Turbulent Transition – Selected Numerical and Experimental Contributions from the DFG-Verbundschwerpunktprogramm "Transition" in Germany*, edited by S. Wagner, M. Kloker, U. Rist, NNFM Vol. 86, Springer, Heidelberg, 2003, 63-74.
28. Panton, R. L., "Overview of the self-sustaining mechanisms of wall turbulence," *Progress in Aerospace Sciences,* Vol. 37, 2001, pp. 341-383.
29. Perry, A. E., and Chong, M. S., "On the mechanism of wall turbulence," *J. Fluid Mech.*, Vol. 119, 1982, pp. 361-388.
30. Robinson, S. K., "Coherent motions in the turbulent boundary layer," *Ann. Rev. Fluid Mech.*, Vol. 23, 1991, pp. 601-639.
31. Samtaney, R., Silver, D., Zabusky, N., and Cao, J., "Visualizing features and tracking their evolution," *Computer,* Vol. 27, 1994, pp. 20-27.
32. Schafhitzel, T., Baysal, K., Vaaraniemi, M., Rist, U., and Weiskopf, D., "Visualizing the evolution and interaction of coherent structures in time-dependent 3D flow," *Transactions on Visualization and Computer Graphics,* Vol. 17, No. 4, 2011, pp. 412-425.
33. Stegmaier, S., Rist, U., and Ertl, T, "Opening the can of worms: An exploration tool for vortical flows", IEEE Visualization Conference 2005.
34. Tanaka, M., and Kida, S., "Characterization of vortex tubes and sheets," *Physics of Fluids A*, Vol. 5, No. 9), Sept. 1993, pp. 2079-2082.
35. Wu, X., and Moin, P., "Direct numerical simulation of turbulence in a nominally-zero-pressure-gradient flat-plate boundary layer," *J. Fluid Mech.,* Vol. 630, 2009, pp. 5-41.
36. Wu, J.-Z., Xiong, A.-K., and Yang, Y.-T., "Axial stretching and vortex definition," *Physics of Fluids*, Vol. 17, No. 3, 038108 (2005).